AL49 - Impact of Metal Pad Heave on Shell Temperature of Aluminum Reduction Cells

André Felipe Schneider[1], Daniel Richard[2] and Marc Dupuis[3]
1. Consultant
2. Associate
Center of Excellence for Aluminum, Hatch Ltd., Montréal, Canada
3. Consultant, GeniSIM, Inc., Saguenay, Canada
Corresponding author: andre.schneider@hatch.com

Abstract

The operational window of an aluminum reduction cell is largely determined by magnetohydrodynamics (MHD) and energy balance. While these two fundamental aspects of cell design are usually studied independently, they are in fact coupled. The ledge profile affects the internal electrical current distribution – and, ultimately, Lorentz Forces – while MHD impacts both the metal pad heave and the flow pattern of the liquid phases. These interactions are commonly neglected in numerical modeling and it is usually assumed that the ledge profile and temperature distribution obtained with a quarter cell energy balance computation are representative of the entire cell. However, it is observed in operating cells that the downstream (DS) sidewall of a typical side-by-side, side riser reduction technology is usually hotter than the upstream (US) one. This suggests a significant relationship between the uneven profile of the interface and the spatial distribution of cell heat flux to the ambient. This article presents a tridimensional (3D) thermoelectrical approach for assessing the impact of a distorted metal pad to bath interface on the potshell temperature distribution of a cell using the modernized ANSYS-based model presented earlier [1, 2]. Key conclusions are illustrated by means of numerical results obtained for a fictitious 375 kA reduction technology.

Keywords: Aluminum reduction cells, Energy balance, Metal pad heaving.

1. Introduction

The operational window of an aluminum reduction cell is largely determined by magnetohydrodynamics (MHD) and energy balance. While these two fundamental aspects of cell design are usually studied independently, they are in fact coupled. The ledge profile affects the internal electrical current distribution – and, ultimately, Lorentz Forces – while MHD impacts both the metal pad heave and the flow pattern of the liquid phases. These interactions are commonly neglected in numerical modeling thus enabling the employment of pure, stand-alone thermoelectrical (TE) numerical analyses to study the energy balance of a Hall-Héroult cell.

Such modeling approaches [1–7] often ignore the local effects of metal pad velocity, alumina concentration, and bubble-driven flow (amongst other phenomena) on the heat transfer between the liquid phases and ledge. It also typically considers uniform heat transfer coefficients along the cell perimeter for each of the distinct ledge regions – namely, the lower ledge (facing metal), the upper ledge (facing bath) and, if considered in the calculations, the ledge trench.

This major simplification – *i.e.*, the dissociation between MHD and energy balance – results in considering a uniform metal pad height during energy balance calculations, inherently neglecting the potential influence of its deformed nature on the overall heat losses distribution. In other words, a double symmetry is assumed, and the heat lost to the ambient by a quarter cell geometry necessarily has to be identical to that of the other 3 quadrants of the full cell.

Considerable efforts have been made [8-11] to better account for the effects of the liquid phases flow on the energy balance of a reduction cell. For instance, Langlois *et al*. (2015) [8] introduced a coupled MHD-TE model that considers the MHD-induced flow while ignoring both the bubble-driven effects on the bath as well as the thermal effects caused by alumina dissolution. Moreover, this same work also assumes a flat heave, based on the following statement:

"It has been shown that the metal-bath deformation has no significant impact on the ledge formation in steady-state."

Once the MHD-driven flow for a given reduction technology is known, a relationship between the latter and the heat transfer between the liquids – especially the metal pad – and the ledge can be established. S. Renaudier and coworkers (2018) [9] validated that MHD-TE modeling approach by employing a procedure consisting of 16 distinct experiments generating a set of calibration parameters suitable for the prediction of ledge formation and cell temperature distribution.

This model was then applied [10] to the calculation of an AP44 potshell temperature profile, as shown in Figure 1. The high temperatures seen on both end walls and upstream (US) shell corners seem to correlate well with the high metal pad velocities observed in these areas. It is worth noticing, however, that the downstream (DS) sidewall also presents high temperatures in the vicinity of the cell center, even though exposed to lower liquid velocities that seem similar to the corresponding US sidewall segment. This might indicate that other phenomena are involved in the observed US-to-DS difference in potshell temperature.

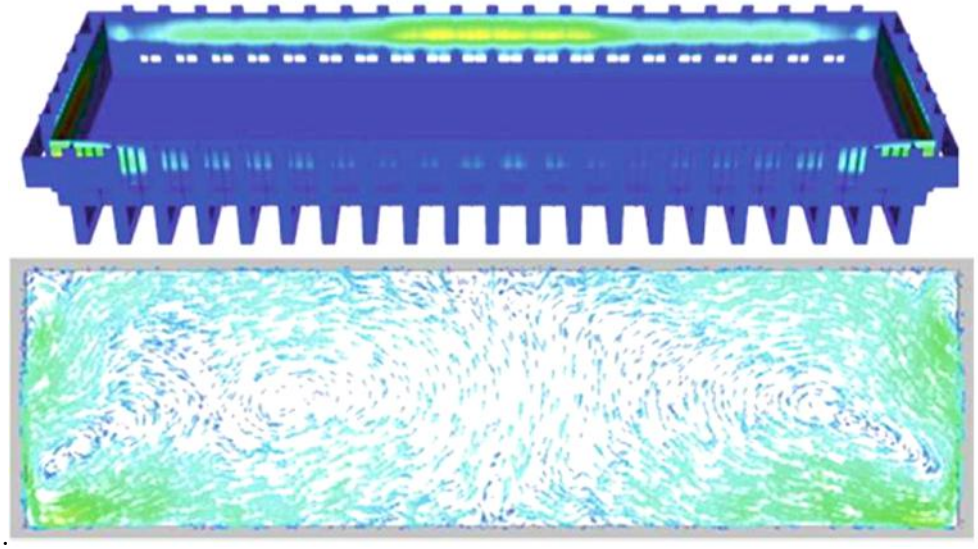

Figure 1. Predicted temperature profile and liquids velocity field for an AP44 cell, where potline current flows from the bottom to the top of the page – reproduced from [10]. Top: potshell temperature (scale not shown), Bottom: velocity field (scale not shown).

One possible explanation may be related to the variation of the metal pad-bath interface elevation on the ledge surface. Metal pad heaving is closely related to the divergence of the Lorentz Forces field such that the interface profile of a typical side-by-side, side risers cell tends to be offset towards the DS sidewall as depicted in Figure 2, with DH being the height difference with respect to the flat interface. It is observed in operating cells that the DS sidewall of such reduction technologies is usually hotter than the US one, similar to that of Figure 1. This suggests the existence of a relationship between the distorted metal pad-bath interface and the spatial distribution of cell heat flux.

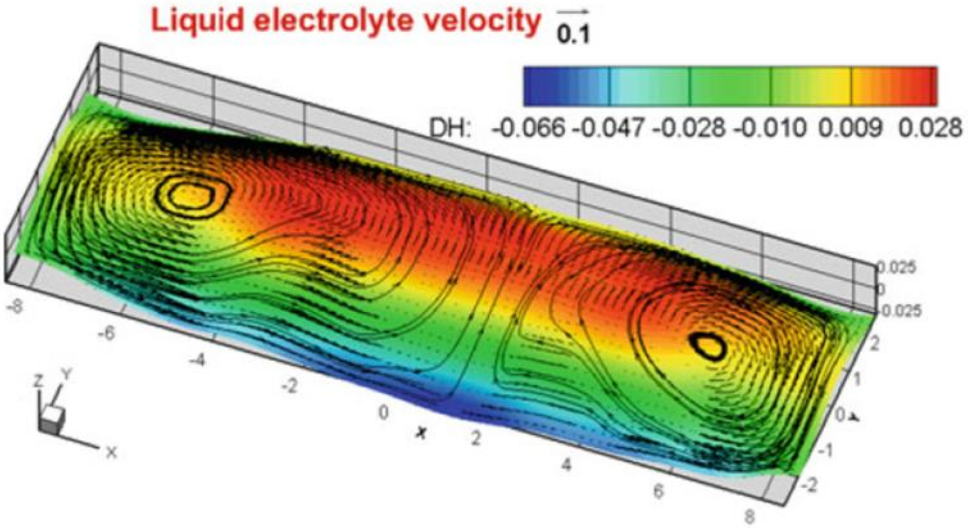

Figure 2. Metal pad-bath interface profile for a typical side-by-side, side risers cell, [m] – adapted from [12]. Potline current flow is in +Y direction.

2. Metal Pad Heaving and Cell Energy Balance

Consider the typical cell cross-section found in Figure 3, where the location of the metal pad-bath interface is denoted by the ledge trench.

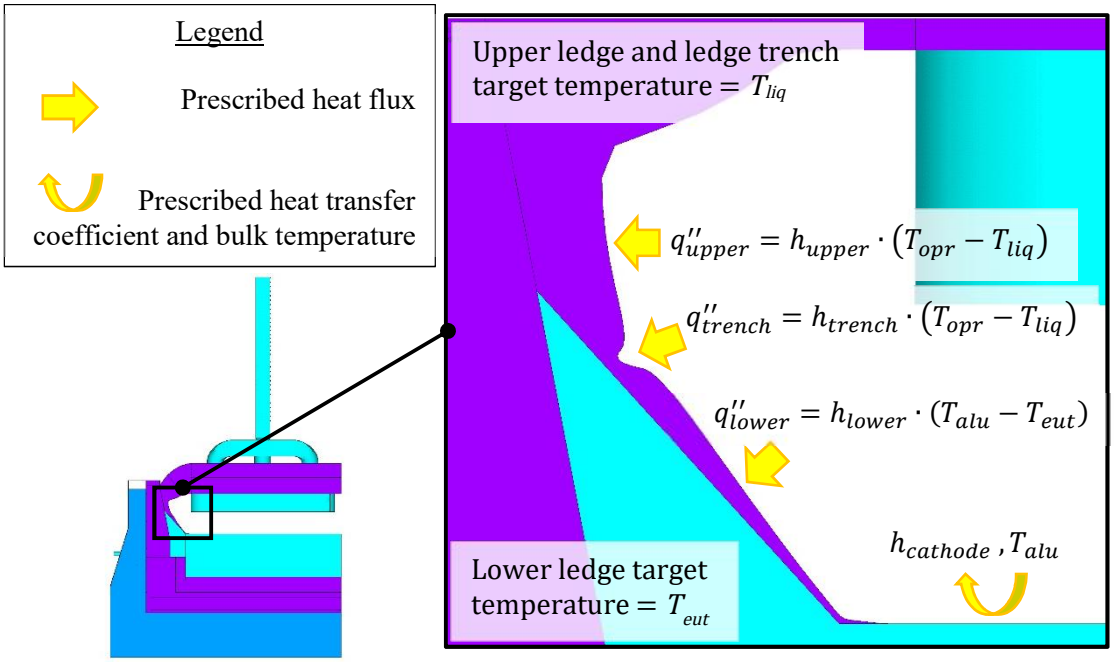

Figure 3. Typical cross-section of an aluminum reduction cell – reproduced from [2].

where:

q''_{upper}	Prescribed heat flux at the upper ledge (facing bath), W/m^2
h_{upper}	Uniform heat transfer coefficient at the upper ledge (facing bath), W/m^2·°C
T_{opr}	Bulk bath temperature, °C
T_{liq}	Liquidus temperature evaluated at the bulk bath composition, °C

q''_{trench}	Prescribed heat flux at the trench region, W/m^2
h_{trench}	Parabolic heat transfer coefficient distribution that varies with the trench height, W/m^2·°C
q''_{lower}	Prescribed heat flux at the lower ledge (facing metal), W/m^2
h_{lower}	Uniform heat transfer coefficient at the lower ledge (facing metal), W/m^2·°C
T_{alu}	Bulk metal pad temperature, °C
T_{eut}	Eutectic point evaluated at the bath film composition (facing metal), °C
$h_{cathode}$	Prescribed uniform heat transfer coefficient at the cathode panel surface, W/m^2·°C.

Let the prescribed heat fluxes at the distinct ledge regions be independent of their location with respect to the cell perimeter while considering that:

$$q''_{trench} > q''_{lower} > q''_{upper} \quad (1)$$

Notice that this is usually the case since the bath liquidus superheat, $\Delta T_{upper} = T_{opr} - T_{liq}$, is lower than the bath film eutectic superheat $\Delta T_{lower} = T_{alu} - T_{eut}$, such that for similar heat transfer coefficients, the computed flux at metal level is higher than that at bath level. The total heat lost through each of those ledge regions is the integral of their prescribed heat fluxes over their respective surface areas – Equation (2).

$$q_{ledge,i,j} = \iint q''_{ledge,i,j} dzdl \quad (2)$$

where:

$q_{ledge,i,j}$	Total heat lost through ledge region *i* facing sidewall *j*, W
$q''_{ledge,i,j}$	Prescribed heat flux at ledge region *i* facing sidewall *j*, W/m^2
z	Elevation, m
l	Cell perimeter, m.

Therefore, if the metal pad-bath interface were flat, the same amount of heat will be extracted from both US and DS sidewalls. However, if one considers that the heave is not uniform along the cell perimeter, the sidewall exposed to the highest average heave height will extract more heat than its counterpart. Thus, the potshell temperature on the higher average heave side is expected to present higher temperatures. Conversely, the opposite side – exposed to a lower average heave perimeter – should present lower average temperatures for the same set of cell-to-ambient heat transfer conditions – Equation (3).

$$T_{wall,j} \sim T_{amb} + \left(\frac{q_{wall,j}}{A_{wall} \cdot \bar{h}_{eqv,wall}} \right) \quad (3)$$

where:

$T_{wall,j}$	Average temperature of sidewall *j*, °C
T_{amb}	Bulk ambient temperature, °C
$q_{wall,j}$	Total heat lost through sidewall *j*, W
A_{wall}	Sidewall surface area, m^2
$\bar{h}_{eqv,wall} = f(T_{wall,j})$	Average equivalent (*i.e.*, convective and radiative) sidewall-to-ambient heat transfer coefficient, W/m^2·°C.

In order to study the apparent link between metal pad heaving and potshell temperature independently from other phenomena such as alumina dissolution, MHD and bubble-driven flows, the authors developed a 3D thermo-electric (TE) Finite Element (FE) modeling approach capable of taking the uneven perimeter of the heave into account when assessing the energy balance of a cell.

3. Implementation in the Modernized TE FE Model

The authors introduced in 2020 a modernized ANSYS-based TE model [1] that builds upon the foundations first introduced and further developed by Dupuis [3–7] from the mid-1980s up to his most recent publications in the 2020s. The prediction of the ledge profile is achieved by means of successive repositioning of the solidification front to solve the Stefan problem. In 2021, a simplified approach for the prediction of the ledge trench (Figure 3) was introduced [2] as well as the capability of considering different bath chemistries, solidification temperatures and superheats for each region of the ledge. In the present work, new features were introduced to explicitly model the uneven heave profile.

3.1 Possible Cell Topologies and Heave Perimeter Repositioning

The range of possible model configurations was expanded for the computation of either slice, quarter, half, or full cell geometries, as shown in Figure 4.

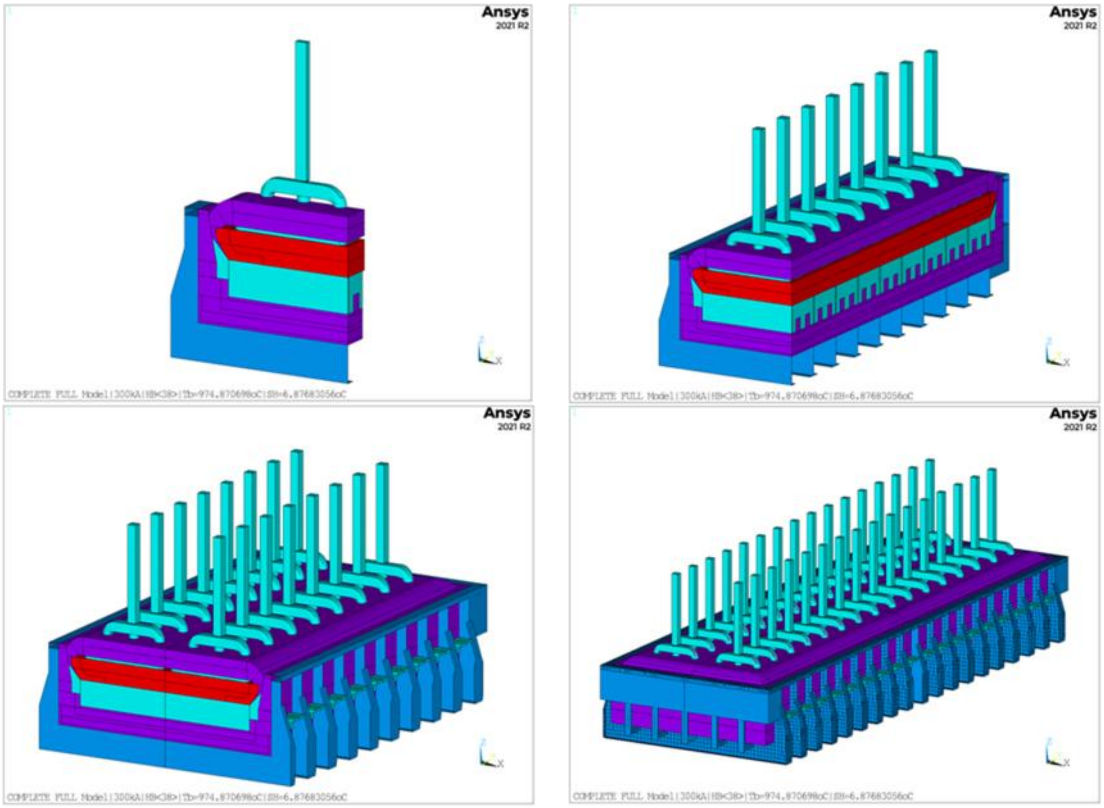

Figure 4. Different FE TE model configurations. Top Left: slice cell geometry, Top Right: quarter cell geometry, Bottom Left: half cell geometry, Bottom Right: full cell geometry.

Starting from a flat metal pad configuration, the interface deformation is imposed in the model mesh from a user-defined height offset along the cell perimeter, which can be obtained either from a MHD analysis or from *in-situ* measurements. Notice that the height of the ledge trench –

if included in the analysis – is kept constant during the mesh repositioning. The mesh of both the moving ledge and the moving liquids is adjusted during the procedure, see Figure 5.

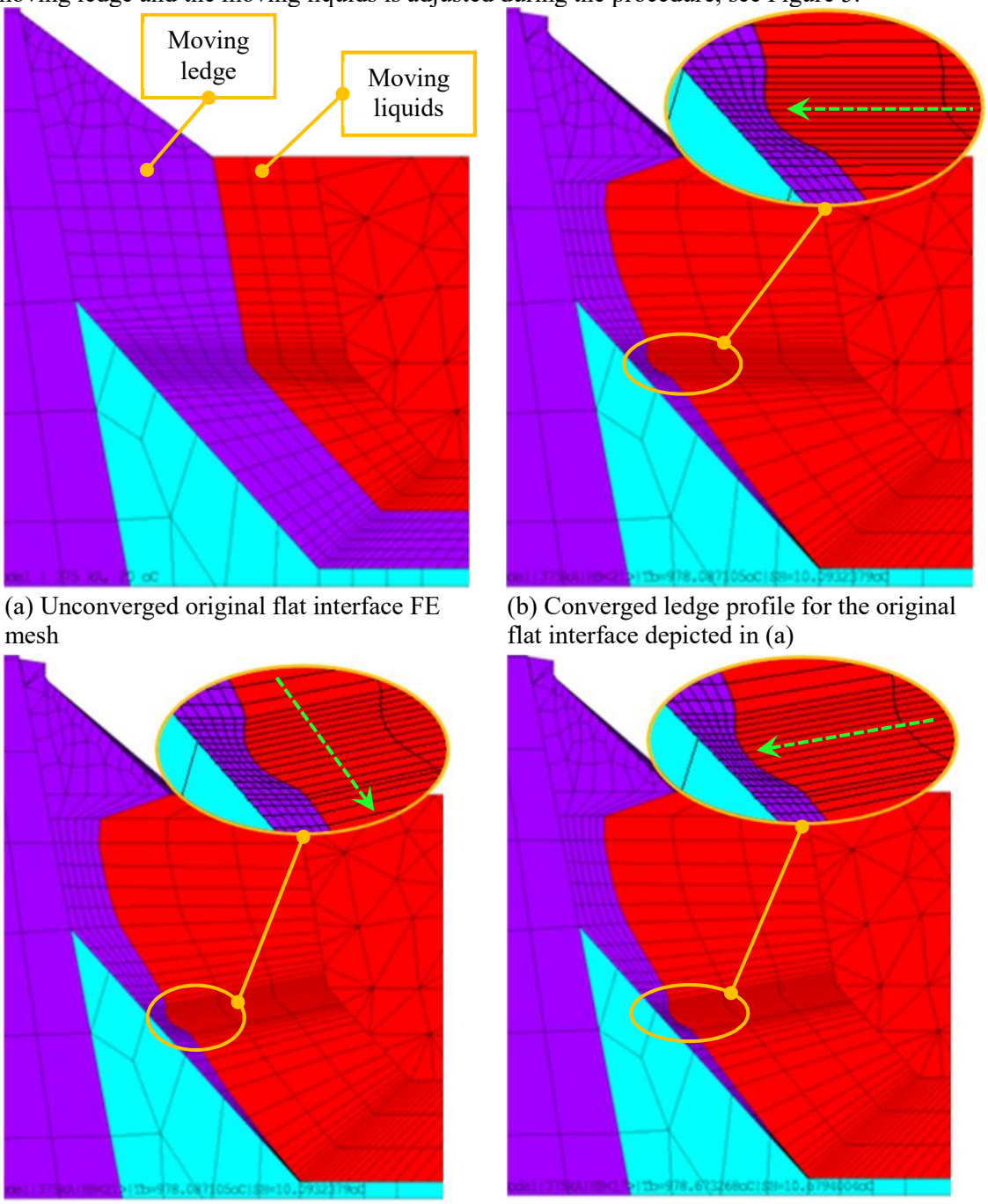

(a) Unconverged original flat interface FE mesh

(b) Converged ledge profile for the original flat interface depicted in (a)

(c) Unconverged FE mesh, repositioned from (b) according to the assumed interface

d) Converged ledge profile for the deformed interface found in (c)

Figure 5. Metal pad-bath interface perimeter repositioning logic, where arrows indicate solidification front displacement.

3.2 Other Notable Improvements

In order to account for the usually non-uniform distribution of collector bar current, an arbitrary profile of collector bar current distribution can be prescribed. For simplicity, the anode bridge is assumed to be equipotential in this work. Finally, a new convergence scheme for the prediction

of the solidification front was devised, which drastically reduced the total amount of FE TE equilibrium iterations by roughly 70 %.

4. Numerical Experiments

To illustrate the impact of metal pad heaving in the energy balance of a cell, four analyses were performed based on the original fictitious 300 kA demonstration cell model found in [2], but now with a redesigned lining and operating at 375 kA, which is more representative of current industry practice.

Starting from a traditional quarter cell geometry with flat metal pad-bath interface and uniform cathodic current, a half cell model under similar conditions was studied. This same half cell geometry was then subjected to the assumed cathodic current distribution shown in Figure 6 and to the deformed metal pad-bath interface perimeter depicted in Figure 7. Finally, a full cell model was computed. Note that the average metal height is the same in all simulations.

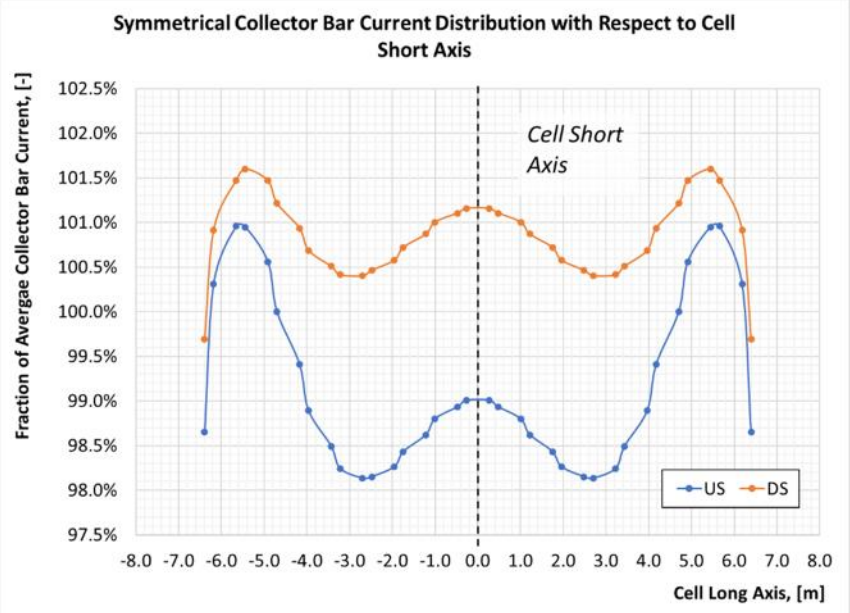

Figure 6. Assumed collector bars current distribution.

Table 1 summarizes the test cases, while Table 2 and Table 3 list the main process and heat transfer parameters, respectively.

Table 1. Description of test cases.

Case #	Topology	Collector Bars Current Distribution	Heave Profile*
1	Quarter cell (Figure 4, Top Right)	Evenly distributed	Flat
2	Half cell (Figure 4, Bottom Left)		
3		As per Figure 6	As per Figure 7
4	Full cell (Figure 4, Bottom Right)		

** An average interface perimeter height of 200 mm was considered for all analyses in order to keep the same total heat loss through the ledge for all cases.*

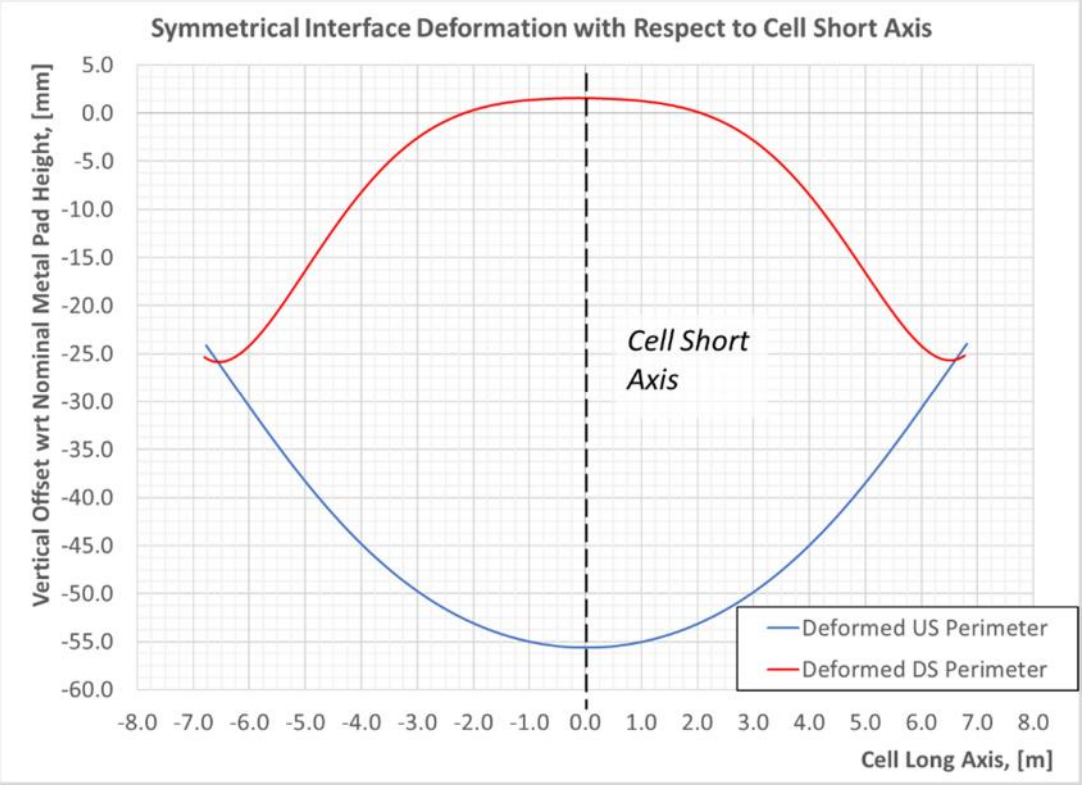

Figure 7. Assumed heave profile along the cell perimeter.

Table 2. Main process parameters.

		Value			
Parameter	**Unit**	**Case 1**	**Case 2**	**Case 3**	**Case 4**
Cell amperage	kA	375.0			
External voltage	mV	200.0			
ACD	mm	35			
Anode cover thickness		160.0			
Ambient temperature	°C	20			

Bulk bath composition		
Excess (dissolved) [AlF_3]	%	10.825
Dissolved [Al_2O_3]		2.500
[CaF_2]		3.000
[LiF]		0.000
[MgF_2]		

Bath film composition		
Excess (dissolved) [AlF_3]	%	3.000
Dissolved [Al_2O_3]		9.100
[CaF_2]		4.000
[LiF]		0.000
[MgF_2]		

Table 3. Heat transfer parameters.

Upper ledge (facing bath) heat transfer parameters		
Uniform heat transfer coefficient, h_{upper}	W/m^2 °C	1320
Bulk temperature	°C	T_{opr}
Solidification front target temperature		T_{liq}

Ledge trench heat transfer parameters			
Parabolic heat transfer coefficient distribution, h_{trench} (function of trench height)			
Lower ledge-to-trench interface	W/m^2 °C	-	h_{lower} = 1320
Ledge trench mid-height			3500
Trench-to-upper ledge interface			h_{upper} = 1320
Bulk temperature	°C		T_{opr}
Solidification front target temperature			T_{liq}

Lower ledge (facing metal) heat transfer parameters		
Uniform heat transfer coefficient, h_{lower}	W/m^2 °C	1320
Temperature difference between metal pad and bulk bath, $\Delta T_{alu} = T_{opr} - T_{alu}$	°C	4.0
Solidification front target temperature	°C	T_{eut}

Cathode panel heat transfer parameters		
Uniform Heat transfer coefficient, $h_{cathode}$	W/m^2 °C	650
Bulk temperature	°C	T_{alu}

Notice that all calculations were performed with the same material properties while considering symmetrical cell-to-ambient heat transfer conditions. Furthermore, the ledge nodes were iteratively repositioned until the root mean square of the solidification front temperature error was below the prescribed RMS convergence norm $\varepsilon_{RMS} \leq 0.5$ °C, with a maximum allowable error for any individual node (*i.e.*, an infinite norm) $\varepsilon_{INF} \leq 2.0$ °C.

4.1 Main Energy Balance Results

Table 4 summarizes the main energy balance results for all four cases. It can be concluded that these cases are comparable.

It is worth mentioning that, despite having considered the heave deformation in Cases 3 and 4, the total heat lost through each one of the distinct ledge regions – *i.e.,* lower ledge (facing metal), upper ledge (facing bath) and ledge trench – is virtually the same for all test cases. Even though

the local height of the metal pad-bath interface varies according to Figure 7 for the last two analyses, the total integrated power along the cell perimeter remains practically identical since both the individual heat transfer coefficients (h_{upper}, h_{trench} and h_{lower}), superheats (ΔT_{upper} and ΔT_{lower}) and average metal pad height remain untouched. This is a direct result from Equation (2). It must be stressed, however, that this would not necessarily be the case if uneven distributions of heat transfer coefficients – possibly dependent on metal pad and bath velocity fields (including bubble driven flow) – were used.

Table 4. Main energy balance results.

Result	Unit	Case 1	Case 2	Case 3	Case 4
Bulk bath temperature, T_{opr}	ºC	976.12	976.12	976.11	976.11
Liquidus temperature evaluated at bulk bath composition, T_{liq}		967.99	967.99	967.99	967.99
Bath superheat, ΔT_{upper}		8.12	8.12	8.11	8.11
Bulk metal pad temperature, T_{alu}	ºC	972.12	972.12	972.11	972.11
Eutectic point evaluated at bath film composition, T_{eut}		956.46	956.46	956.46	956.46
Metal pad superheat, ΔT_{lower}		15.66	15.66	15.65	15.65
Cell internal heat	kW	828.98	829.98	828.97	828.97
Anode heat losses		263.19	263.19	263.19	263.19
Cathode heat losses		565.79	565.79	565.78	565.78
Bath-to-upper ledge heat losses		87.74	87.75	87.67	87.65
Liquids-to-trench heat losses		31.91	31.92	31.86	31.86
Metal pad-to-lower ledge heat losses		230.02	229.85	230.30	230.23
Metal pad-to-cathode panel heat losses		87.12	87.28	86.94	87.65
Total cell heat losses		828.97	828.98	828.96	828.97
Anode voltage drop	mV	426.17	426.17	426.16	426.16
Cathode voltage drop		337.99	337.99	337.96	337.96
Cell heat imbalance	kW	7.1E-3	4.4E-5	7.1E-3	9.4E-9
Ledge RMS temperature norm*, **	ºC	0.12	0.15	0.12	0.12
Ledge INFINITE temperature norm**, ***		1.35	1.80	1.49	1.57

** Refers to the root mean square difference computed with the local ledge melting temperature for all eligible nodes at the ledge-liquids interface.*

*** All those nodes where the ledge is locally melted (*i.e.*, switched to liquid aluminum) are excluded from error assessment.*

**** Refers to the maximum absolute computed difference with the local ledge melting temperature for an individual eligible node at the ledge-liquids interface.*

4.2 Implementation of New FE TE Model Topologies

Figure 8 and Figure 9 show, respectively, the computed potshell temperature distributions for Cases 1 and 2 while Figure 10 compares the ledge profiles at the symmetry plane coincident with the cell short axis (from now on simply referred to as "symmetry plane"). Evidently, the computed temperature and ledge results are identical, given that all cell-to-ambient heat transfer boundary conditions, internal heat generation, heave profile and current distributions are symmetrical. Furthermore, note that a complete cell model under these conditions would lead to the same results.

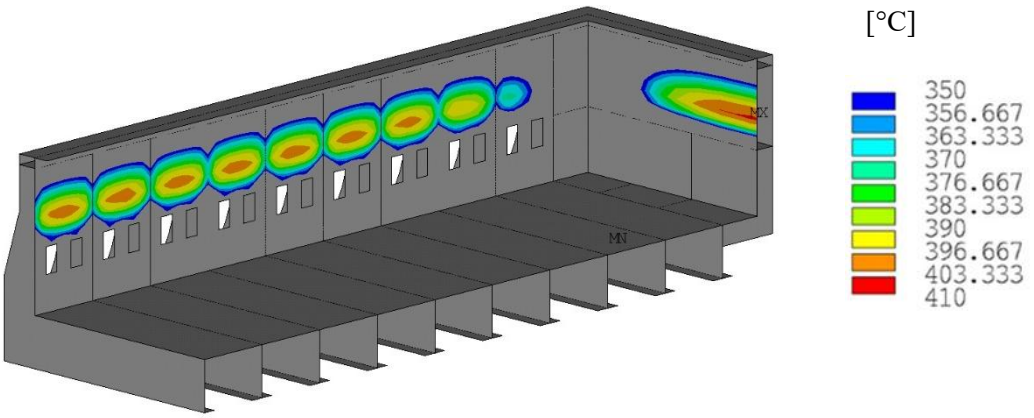

Figure 8. Potshell temperature distribution for Case 1.

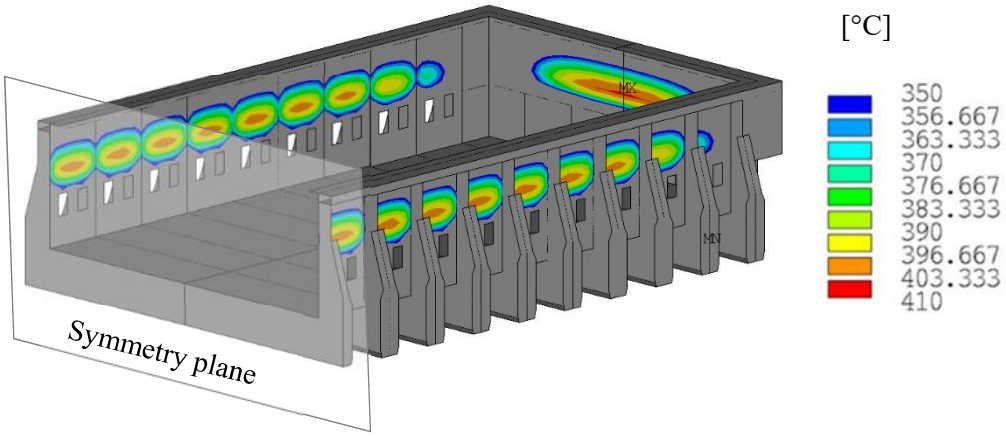

Figure 9. Potshell temperature distribution for Case 2.

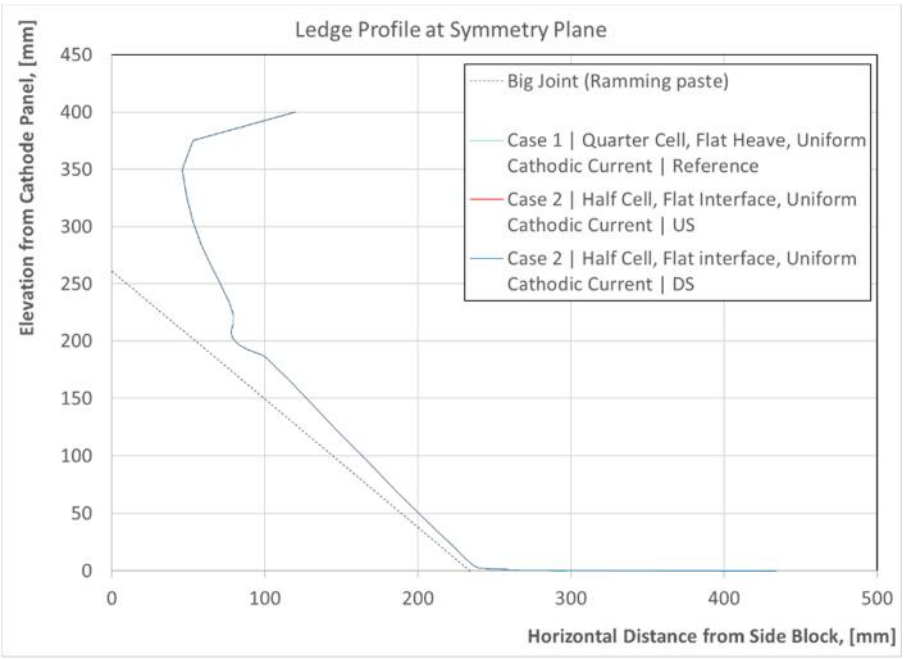

Figure 10. Comparison of heave profiles at symmetry plane for Cases 1 and 2.

It is therefore concluded that the new (*i.e.*, half and full) FE TE model topologies were successfully implemented.

4.3 Impact of Metal Pad Heaving

Figure 11 shows the computed potshell temperature distributions for Case 3 while Figure 12 shows the differences observed between US and DS sides by computing the differences in averaged results evaluated along vertical lines above the collector bar openings. The deformation of the interface (refer to Figure 7) introduces a noticeable difference (about 10 °C) between US and DS sidewalls at the vicinity of the symmetry plane when considering uniform heat transfer coefficients for each individual ledge region, as per Figure 3. The DS ledge loses more heat than its US counterpart given its higher average heave perimeter, as per Equation (2). As such, when subjected to symmetrical cell-to-ambient heat transfer conditions, the DS sidewall is necessarily hotter – refer to Equation (3).

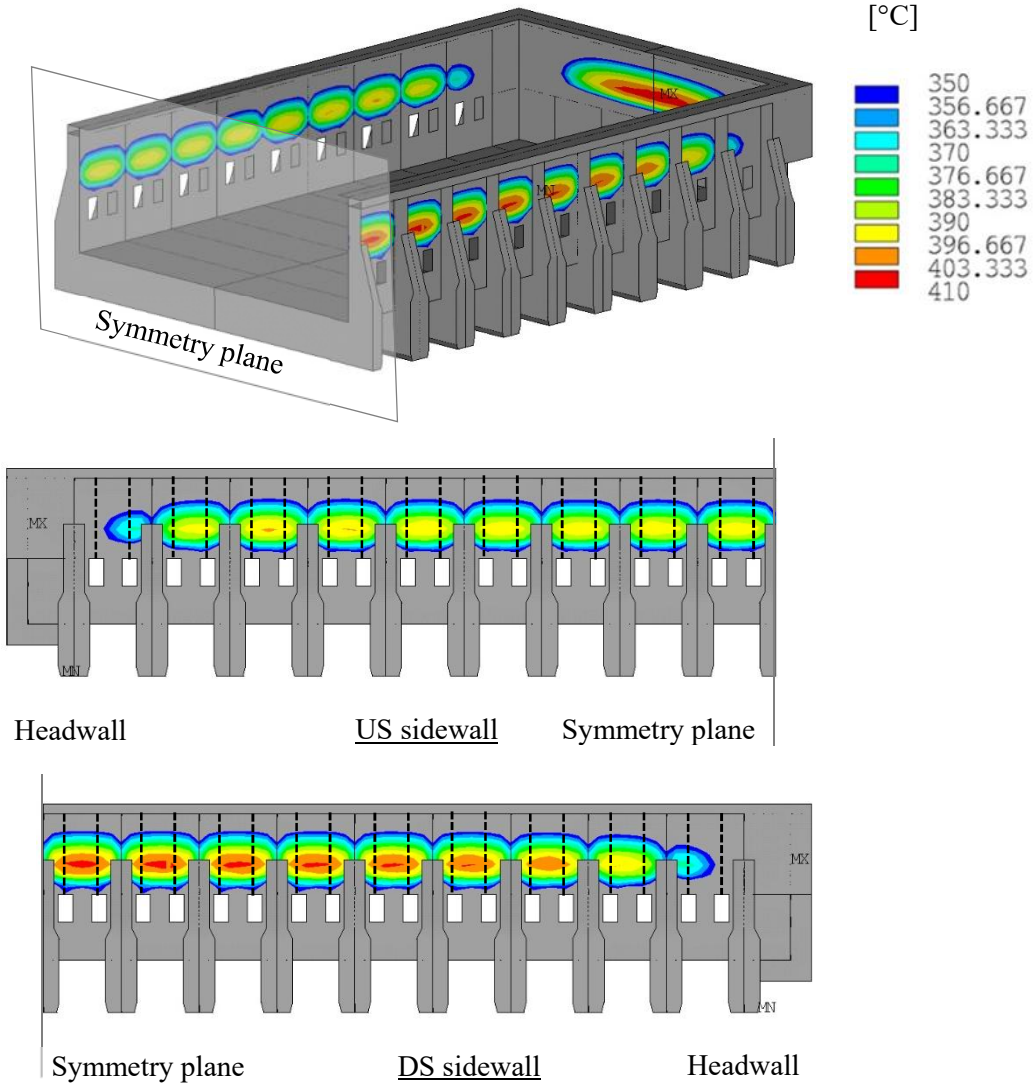

Figure 11. Potshell temperature distribution for Case 3, where dashed lines represent paths for assessing the average side wall temperature above each collector bar. Top: perspective view. Center: US sidewall. Bottom: DS sidewall.

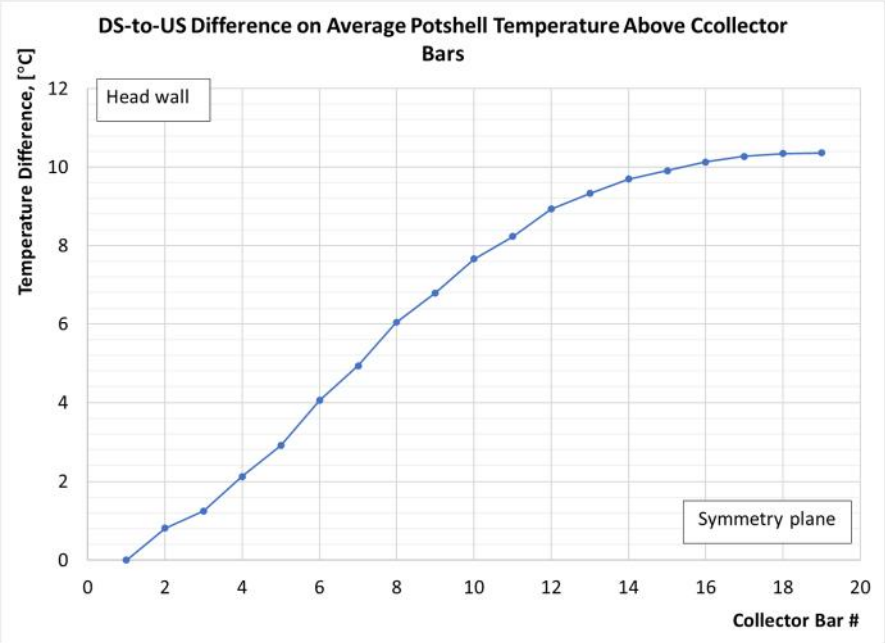

Figure 12. US-to-DS difference in sidewall temperature based on averaged values evaluated along vertical paths above collector bar.

Figure 13 compares the ledge profiles at the symmetry plane for both Cases 1 and 3, where the vertical location of the interface perimeter can be inferred by the ledge trench. Given that all analyses led to the same internal heat generation, operating temperature and cathode voltage drop (CVD), the ledge toe as well as most of the lower ledge (facing metal) profile are virtually the same as they are far removed from the metal pad-bath interface.

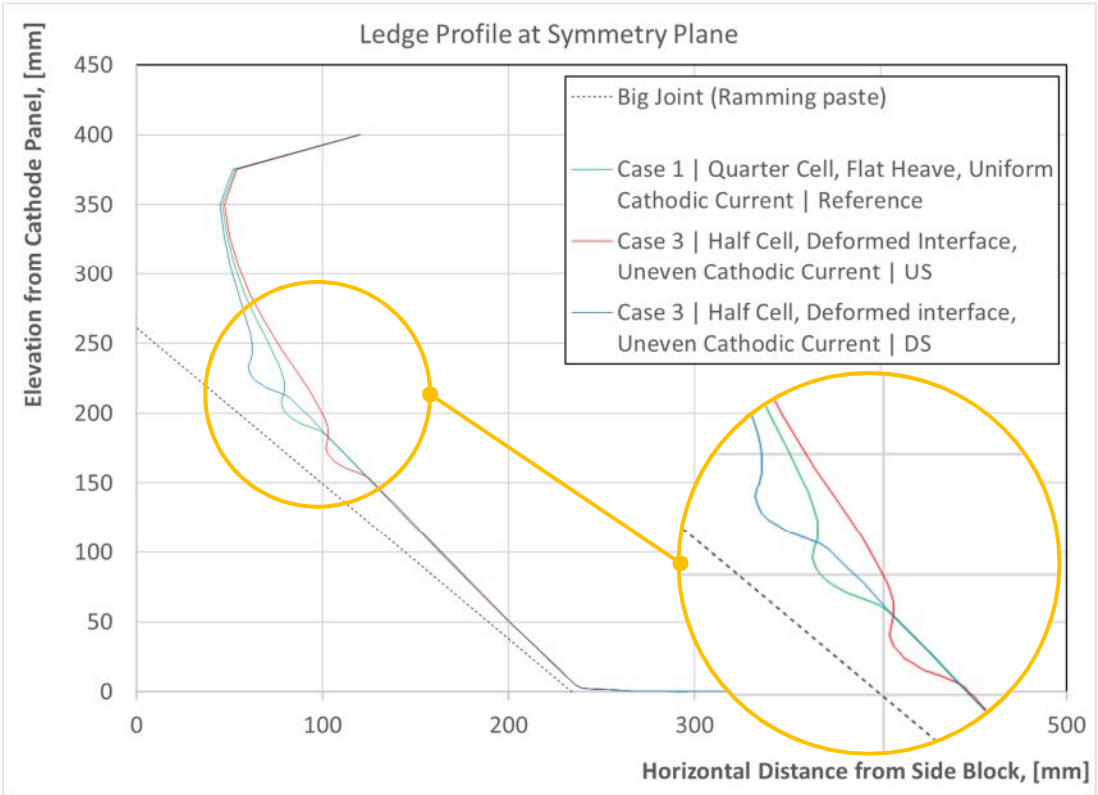

Figure 13. Comparison of ledge profiles at symmetry plane for Cases 1 and 3.

It is interesting to notice, however, that these results partially contradict the previously discussed statement by Langlois et al. (2015) [8], *i.e.,* that metal pad heaving is irrelevant to the prediction of the ledge: by moving the interface either up or down, the ledge locally grows respectively thicker or thinner at the trench vicinity.

Finally, Figure 14 shows the predicted potshell temperature distribution for Case 4, which, as expected, is identical to that obtained for Case 3, given the symmetrical nature of the problem at hand. Furthermore, notice that the resulting ledge profiles are also identical to those obtained for Case 3.

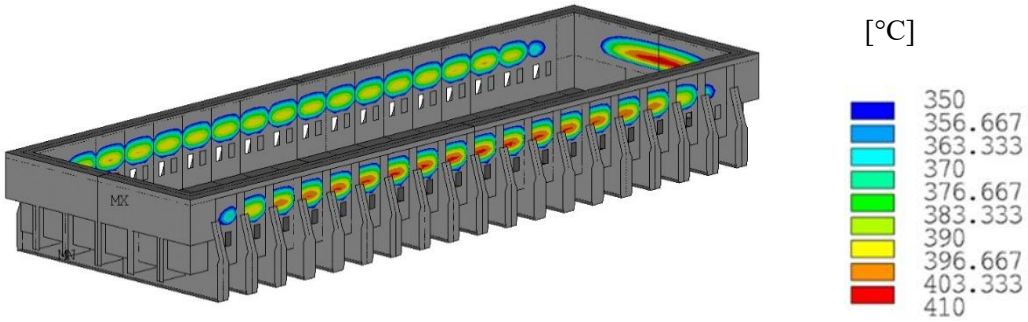

Figure 14. Potshell temperature distribution for Case 4.

5. Conclusions

A FE TE modeling approach explicitly including the metal pad-bath interface distortion was developed and implemented into the modernized ANSYS-based TE model for cell energy balance. Simple electrical boundary conditions were used, but cell-to-cell busbars may be included if needed, as per [13], to obtain an accurate collector bar current distribution rather than assuming one.

It was found that metal pad heaving is, at least, partially responsible for the US-to-DS differences in potshell temperature typically observed in side-by-side, side risers cells, and would help to explain the elevated shell temperature in the center of the downstream side where low liquid velocities are expected. This was demonstrated while considering uniform distributions of liquids-to-ledge heat transfer coefficients for each distinct ledge region and symmetrical cell-to-ambient heat transfer conditions.

The typical elevated shell temperatures in the upstream corners might be explained by the high expected liquids velocities [10]. Appropriate heat transfer coefficients between liquid phases and ledge would be required to reproduce this effect in the TE model.

Calculations have shown that the energy balance of the cell is not affected by the deformation of the metal pad-bath interface as long as:

- The considered heat transfer coefficients for each distinct ledge region (h_{upper}, h_{trench} and h_{lower}) are uniform along the cell cavity perimeter, and;
- The average metal pad perimeter height remains identical to that of a traditional quarter cell TE model.

Notice, however, that this would not necessarily be the case if uneven distributions of heat transfer coefficients – possibly dependent on metal pad and bath velocity fields (including bubble driven flow) – were used.

It was also found that metal pad heaving slightly modifies the ledge profile at the vicinity of the ledge trench, making it thicker or thinner when moving the metal pad-bath interface up or down, respectively.

Finally, the present modeling approach was also extended to handle different topologies, including slice, half and full cell models, allowing for its potential coupling with a MHD model.

6. References

1. Daniel Richard et al., A modernized ANSYS-based finite element model for the thermal-electrical design of aluminum reduction cells, *Proceedings of the 38th International ICSOBA Conference*, Virtual Event, 16 – 18 November, 2020, Paper AL03, *Travaux* 49, 563-580.
2. André Felipe Schneider et al., A Thermoelectrical approach for the modelling of different ledge regions in aluminum reduction cells, *Proceedings of the 39th International ICSOBA Conference*, Virtual Event, 22 – 24 November, 2021, Paper AL20, *Travaux* 50, 835-853.
3. Marc Dupuis and Imad Tabsh, Thermo-electric coupled field analysis of aluminium reduction cells using the ANSYS parametric design language, *Proceedings of the ANSYS Fifth International Conference*, Vol 3, 1991, 1780-1792.
4. Marc Dupuis, Thermo-electric design of a 400 kA cell using mathematical models: a tutorial, *Light Metals* 2000, 297-302.
5. Marc Dupuis, Computation of aluminium reduction cell energy balance using ANSYS® finite element models, *Light Metals* 1998, 409-417.
6. Marc Dupuis, Computation of accurate horizontal current density in metal pad using a full quarter cell thermo-electric model, *Proceedings of CIM* 2001, 3-11.
7. Marc Dupuis, How to limit the heat loss of anode stubs and cathode collector bars in order to reduce cell energy consumption, *Light Metals* 2019, 521-531.
8. S. Langlois et al., 3D coupled and thermo-electrical modelling applied to AP Technology pots, *Light Metals* 2015, 771-775.
9. Steeve Renaudier et al., Alucell: a unique suite of models to optimize pot design and performance, *Light Metals* 2018, 541-549.
10. Pascal Thibeault et al., AP44 development at Alma, *Light Metals* 2018, 737-744.
11. Hongliang Zhang et al., Numerical investigation of flow field effect on ledge shape in aluminum reduction cell by coupled thermos-flow model, *Light Metals* 2020, 517-526.
12. Valdis Bojarevics and Marc Dupuis, Advanced alumina dissolution modelling, *Light Metals* 2022, 339-348.
13. André Felipe Schneider, Daniel Richard, and Olivier Charette, Impact of Amperage Creep on Potroom Busbars and Electrical Insulation: Thermal-Electrical Aspects, *Light Metals* 2011, 525-530.